A micromirror array with annular partitioning for high-speed random-access axial focusing

Nathan Tessema Ersumo[1,2], Cem Yalcin[2], Nick Antipa[2], Nicolas Pégard[3], Laura Waller[1,2,4], Daniel Lopez[5], and Rikky Muller[*1,2,4]

[1] University of California, Berkeley - University of California, San Francisco Graduate Program in Bioengineering, USA

[2] Departement of Electrical Engineering & Computer Sciences, University of California, Berkeley, CA 94720, USA

[3] Department of Applied Physical Sciences, University of North Carolina at Chapel Hill, Chapel Hill, NC 27514, USA

[4] Chan Zuckerberg Biohub, San Francisco, CA 94158, USA

[5] Physical Measurement Laboratory, National Institute of Standards and Technology, Gaithersburg, MD 20899, USA

* Corresponding author

Abstract

Dynamic axial focusing functionality has recently seen widespread incorporation in microscopy, augmented/virtual reality (AR/VR), adaptive optics, and material processing. Yet the limitations of existing varifocal tools continue to beset the performance capabilities and operating overhead of the optical systems that mobilize such functionality. The varifocal tools that are the least burdensome to drive (ex: liquid crystal, elastomeric or optofluidic lenses) suffer from low (~100 Hz) refresh rates. Conversely, the fastest devices sacrifice either critical capabilities such as dwelling capacity (ex: acoustic gradient lenses or monolithic micromechanical mirrors) or low operating overhead (ex: deformable mirror arrays). Here, we present a general-purpose random-access axial focusing device that bridges these previously conflicting features of high speed, dwelling capacity and lightweight drive by employing low-rigidity micromirrors that exploit the robustness of defocusing phase profiles. Geometrically, the device consists of an 8.2 mm diameter array of piston-motion, 48 μm-pitch micromirror pixels that provide 2π phase shifting for wavelengths shorter than 1 100 nm with 10-90% settling in 64.8 μs (i.e. 15.44 kHz refresh rate). The pixels are electrically partitioned into 32 rings for a driving scheme that enables phase-wrapped operation with circular symmetry and requires less than 30 V/channel. Optical experiments demonstrated the array's wide focusing range with a measured ability to target 29 distinct, resolvable depth planes. Overall, the features of the proposed array offer the potential for compact, straightforward methods of tackling bottlenecked applications including high-throughput single-cell targeting in neurobiology and the delivery of dense 3D visual information in AR/VR.

Introduction

With the increasingly broad reliance on volumetric processing for improved throughput and precision in optical systems, dynamic axial focusing has recently emerged as an essential feature across several

disciplines. Accordingly, varifocal tools have become common fixtures in applications including biological microscopy[1], immersive displays[2], ophthalmoscopy[3], astronomy[4], and material processing[5]. In neurobiology, for instance, achieving single-cell resolution targeting across tissue volumes with densities of up to 10^5 neurons/mm^3 and thicknesses of up to 1 mm requires dynamic access to several depths at speeds that are commensurate with the millisecond timescales of neural signaling[1,6,7]. Similarly, in augmented and virtual reality (AR/VR), accommodating depth cues for 3D images entails the use of axial focusing tools[2]. Furthermore in AR/VR, these tools can alleviate the burden posed by the delivery of dense 3D visual information via high-speed depth-based frame partitioning schemes that exploit the 1 kHz physiological detection rate of the human eye[8].

Currently, the most prevalent approaches to dynamic axial focusing achieve focus tuning by deforming or reorienting optofluidic[9,10], elastomeric[11] or liquid crystal-based[12] lens components. While such technologies offer straightforward actuation mechanisms, their lagging performance capabilities are increasingly apparent relative to accompanying optical components, especially lateral scanning tools that are often used in conjunction with axial focusing for joint 3D scanning capability[1]. Specifically, while optofluidic and elastomeric lenses remain well below the 1 kHz speed threshold needed to achieve sub-millisecond response times even under optimized conditions[13], state-of-the art lateral scanning tools such as galvanometers routinely achieve refresh rates of tens of kHz[14]. Liquid crystals lenses also suffer from similar speed bottlenecks with the added constraint of having polarization-dependent functionality[15]. In a telling illustration of these stark performance mismatches, recent efforts have even resorted to converting galvanometer-based lateral steering into axial focusing using a custom-designed reflective surface[16].

A general strategy for speeding up axial focusing has been to employ rapidly oscillating systems to continuously sweep across a range of depths. One such approach is the tunable acoustic gradient index of refraction (TAG) lens, which produces a radial pattern of standing acoustic waves to a fluid chamber

in order to create continuous changes in refractive index that can achieve focus sweeping at rates on the order of 100 kHz[17]. A second approach takes cue from galvanometric scanners by employing reflective mechanical structures and adapting them to axial scanning by trading tilting resonance modes for ones that produce radial curvature[18,19]. However, the oscillatory behavior that enables such speeds has also proven restrictive as it precludes the capacity for dwelling, which is crucial to applications that require short switching times followed by longer hold durations at specific depths. For example, signal-to-noise ratio (SNR) considerations in some imaging systems impose a minimum bound on sensor pixel dwell time that often requires several oscillation periods with such continuously scanning tools[20]. Moreover, some optical systems may rely on kinetics that cannot trade optical power linearly against exposure time[21]. Unlike TAG lenses, micro-electromechanical systems (MEMS) are opportunely positioned to circumvent this constraint because high mechanical resonance frequencies translate to rapid settling times under DC actuation with proper damping conditions[22]. Additionally, under electrostatic actuation, MEMS devices are considerably less susceptible to gravity-induced optical aberrations and less sensitive to mechanical vibrations compared to fluidic or elastomeric systems[23].

Nevertheless, some remaining challenges must be addressed in order to adapt axial focusing MEMS tools to dwelling-capable operation. Monolithic mirror plates designed to be operated at resonance cannot achieve meaningful actuation at DC without excessively high voltage drives on the order of 100 V or more[18,19]. Furthermore, such structures can often only be actuated in one direction, typically only producing concave curvatures that restrict resulting dioptric powers to positive ranges[18,19]. One solution to these challenges is to partition the active MEMS array in an annular fashion into independently addressable rings as illustrated in Fig. 1. This strategy, which has seen increased consideration and adoption in recent years[24,25], reduces the required displacement range, and therefore also the driving range, by exploiting phase-wrapping capabilities as each actuated element would only need to produce a total phase shift of 2π. Under such schemes, the dioptric power range is no longer limited by

mechanical compliance bounds and driving limitations, but rather the gradual drop in efficiency that comes from applying discrete phase profiles of increasing gradient[26] as target depth is moved further away from the default focal plane set by the accompanying offset lens (Fig. 1b). Annular partitioning schemes can also tackle recurring issues in wavefront shaping. Namely, the expanded level of control that discrete independent rings provide can eliminate radial aberrations from imperfect phase profiles produced by axial focusing tools[27] as well as spherical aberrations from other components in the optical system[28], both of which would require complex optics for tailored correction. In addition, annular partitioning can accommodate requirements for simultaneous targeting of multiple depths by allotting subsets of rings to different target depths[29].

Despite such benefits, annular geometries suffer from drawbacks that have led some to favor alternative partitioning schemes. Specifically, annular concentric structures vary significantly in size, leading to non-uniform actuation behavior that complicates driving and settling schemes. Moreover, size, shape and suspension schemes across such structures can introduce varying levels of torsional instability and residual stress mismatches resulting in buckling or curling[30]. Given these considerations, a two-dimensionally periodic array of identical segmented micromirrors or of identical mechanically intercoupled deformable mirrors, numerous versions of which have been developed over the years[31,32], could offer a better partitioning scheme. Admittedly, periodic geometries increase the proportion of non-active areas across the illuminated aperture region, thereby introducing static diffraction patterns and decreasing the active diffraction efficiency set by the square of the fill factor[33]. However, such impacts can be mitigated by adopting any of the several tactics that are routinely employed today with pixelated spatial light modulators, including fill factor maximization, amplitude masking and spatial filtering[34,35].

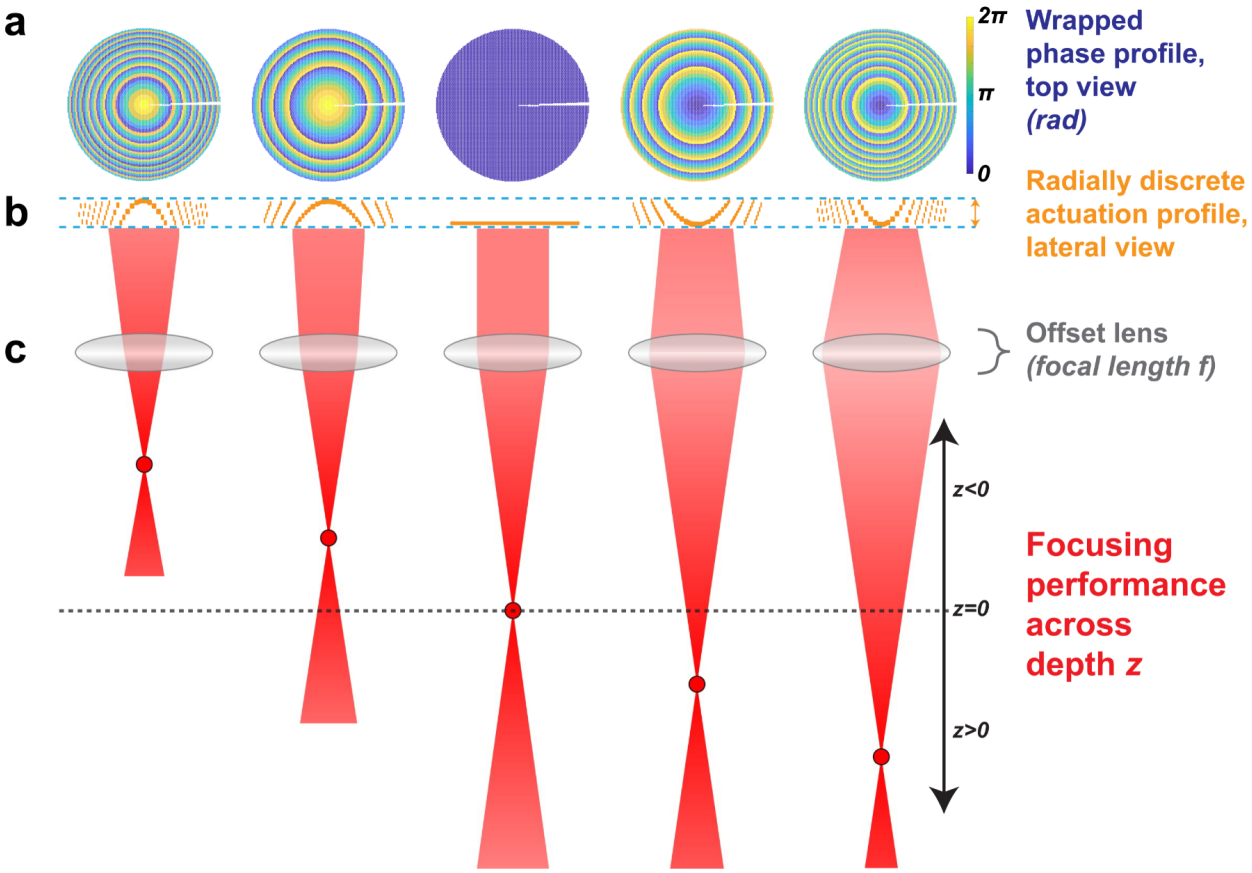

Fig. 1. *Schematic diagram illustrating the principle of operation of a radially partitioned varifocal micromirror array. By actuating independently addressable rings, phase-wrapped concave and convex phase profiles may be produced in order to dynamically focus light to different depths along the optical axis z. An offset lens of a given focal length f is used in conjunction with the array in order to focus at a default position z=0 when the phase is kept uniform across all rings of the array.*

In summary, the fast response times and uniform actuation behavior of small unit structures make pixel partitioning preferable to annular partitioning[31]. However, a survey of currently available MEMS arrays reveals that existing array-based solutions are not ideally suited for adaptation to nimble and general-purpose axial focusing. The broadly used digital micromirror devices (DMDs), for instance, which offer binary amplitude modulation, have been employed to target multiple depths via the generation of

Fresnel zone plates, but the generation of foci at symmetric orders and efficiencies on the order of 1% make such tools impractical for axial focusing[36]. Deformable mirror arrays, on the other hand, are subject to inter-actuator coupling, which impedes radial phase wrapping, and utilize highly rigid suspension schemes that raise voltage drive requirements to hundreds of volts across hundreds of actuation channels, creating significant operating overhead[37,38].

Hence, the need for a high-speed axial focusing tool with reasonably light operating overhead and features for general-purpose use (including independence to polarization, operability across a wide wavelength range and dwelling capacity) remains unmet. Here, we demonstrate a micromirror-based system that satisfies these requirements by striking a balance between annular partitioning for discrete radial phase control and 2D periodic micromirror tiling for uniform and high-speed actuation behavior. A circular micromirror array forms the active area of the focusing tool, and simple voltage-driven parallel-plate electrostatic actuation produces the piston motion required for phase shifting across the array's 23 852 micromirror pixels[39,40]. Importantly, the micromirrors were electrically wired into 32 independently addressable annular rings and micromirror suspension rigidity was relaxed for low-voltage drive (<30 V). Compact integration to a 32-channel off-the-shelf digital to analog converter (DAC) therefore allows us to achieve full focusing operation with a straightforward and uniform driving scheme. While the higher sensitivity of the suspension scheme increases susceptibility to process variations and results in some deviation in actuation behavior across pixels, the primitive nature of radially varying discrete-step phase profiles allows us to benefit from the averaging effect of having up to hundreds of pixels in a given ring. In addition, the pixel structure and tiling scheme were designed to ensure a systematic wiring process that maintains micromirror planarity under conformal deposition constraints and to provide mechanical stops that prevent electrode contact. Lastly, mirror stroke was designed to allow for 2π phase shifting across wavelengths of up to 1 100 nm for a spectral range that encompasses ultraviolet, visible and part of the near-infrared regions.

Results

Pixel-level fabrication

MEMSCAP's PolyMUMPs and MUMPs-PLUS platforms were used to produce the focusing array, with custom post-processing performed for reflective layer deposition. Fabrication steps, micromirror structure and tiling geometry are shown in Fig. 2. A unit pixel is a 48 μm-pitch electrically grounded micromirror plate suspended with two clamped-guided beams over a fixed driving electrode. This micromirror geometry was patterned from three polysilicon layers and one gold metal layer for reflectivity, with electrical routing and fixed driving electrodes confined to Polysilicon 0. As part of MEMSCAP's MUMPs-PLUS option for semi-custom modifications, the Polysilicon 1 layer, which forms the body of the suspension beams, was thinned down from the 2 μm standard of the PolyMUMPs process to 0.5 μm in order to reduce spring stiffness and lower voltage drive requirements. To reinforce the body of the micromirror plate and prevent curling due to residual stress mismatches, the suspended mirror bodies were patterned from a double stack of Polysilicon layers 1 and 2. As an accompanying step in stress mitigation, custom evaporation and lift-off post-processing was performed to reduce the thickness of the reflective gold layer from the 500 nm standard of the PolyMUMPs process to 250 nm.

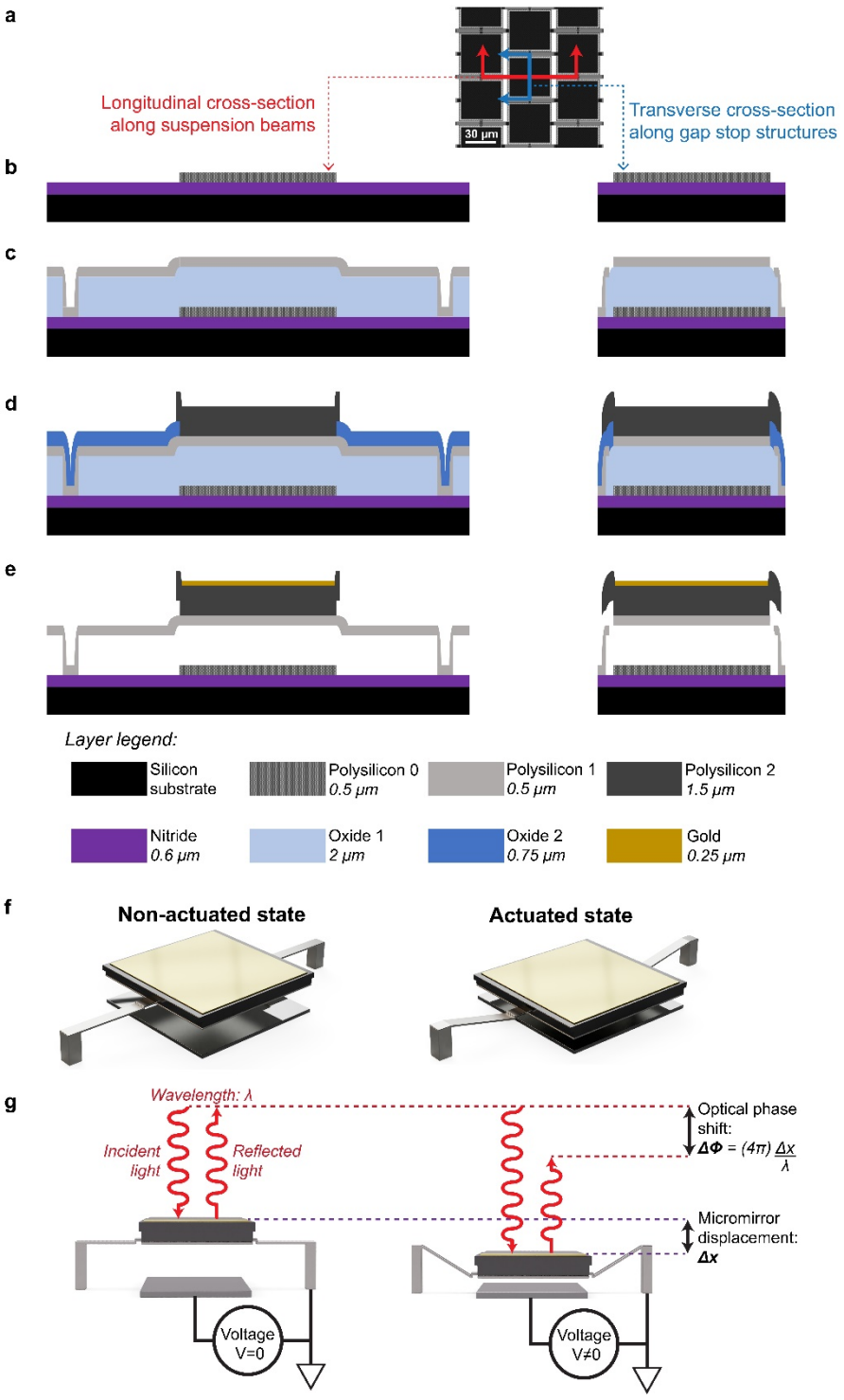

Fig. 2. *Fabrication and actuation principle of unit micromirror pixels. (**a**) Top-view of orthogonally staggered pixel tiling geometry with locations of fabrication cross-sections in b-e denoted by colored lines. (**b-e**) Fabrication cross-sections after the deposition and patterning of the following layers: (**b**)*

*Polysilicon 0, (**c**) Polysilicon 1, (**d**) Polysilicon 2, and (**e**) gold. (**f-e**) Isometric and sagittal views of micromirror renderings at rest and under actuation with exaggerated scale along direction of displacement.*

The conformal nature of deposition steps in the PolyMUMPs process introduces a top-to-bottom planarity constraint which prevents the patterning of suspension beams and anchors underneath the active region of each mirror plate. Accordingly, a gold metal surface area of 40 x 40 μm^2 was allocated for each pixel (Fig. 2e-f) and an orthogonal array format with a staggered tiling scheme was chosen in order to accommodate non-overlapping suspension beams that extend into adjacent pixels (Fig. 2a). In addition to extending the length of suspension beams for further stiffness reduction, this tiling scheme prevents electrode contact in the event of electrostatic pull-in or pixel failure. This capability is achieved by having suspension beam anchors serve as gap stops for overhanging juts that are strategically placed to protrude from the Polysilicon 2 layer of adjacent mirror bodies (Fig. 2e). Thus, while the 2 µm size of the electrode gap triggers pull-in past a mirror displacement of 667 nm under electrostatic voltage drive, the mechanical stops cap maximum displacement at 750 nm, at which point a reduction of the applied voltage below the pull-out threshold restores the mirror back to a regular operating regime. The overhanging juts were sized to be large enough to accommodate the requisite mask misalignment tolerance for the PolyMUMPs process but small enough to avoid contact with neighboring juts such that mirror bodies are physically isolated from each other at all times. Altogether, our pixel-level micromirror structure and complementing tiling scheme efficiently exploit the space and material made available by the fabrication process in order to produce a robust actuation scheme that abides by planarity and feature size constraints. The relationship between this electrostatic actuation scheme and optical phase shifting is illustrated in Fig. 2g: the piston-motion actuation of a given mirror increases the optical path of locally incident light, adding twice the actuation displacement to the travel distance.

Top views of fabricated arrays in Fig. 3 further illustrate how the chosen pixel and tiling geometries also incorporate an efficient architecture for pixel wiring with minimal footprint. Traces connecting rings to bond pads were placed together within a dedicated 7.2° radial slice in order to minimize routing placement overhead and keep area usage consistently at 2% regardless of the chosen size and pixel count of the circular array (Fig. 3a,b). Importantly, wiring between adjacent pixels belonging to the same ring is ensured via 8 potential pixel-level connection points whose placement/omission does not impact mirror planarity as shown in Fig. 3c. This connection scheme also allows for an automated placement process during layout once the exact ring partitioning geometry is chosen. Lastly, as part of our structural inspection of the fabricated arrays, topography measurements using atomic force microscopy (AFM) were performed to evaluate the quality of the custom-deposited reflective gold layer. No planarity issues were noted and height variation across 50x50 nm^2 unit regions of gold surface had a standard deviation of 12.09 nm.

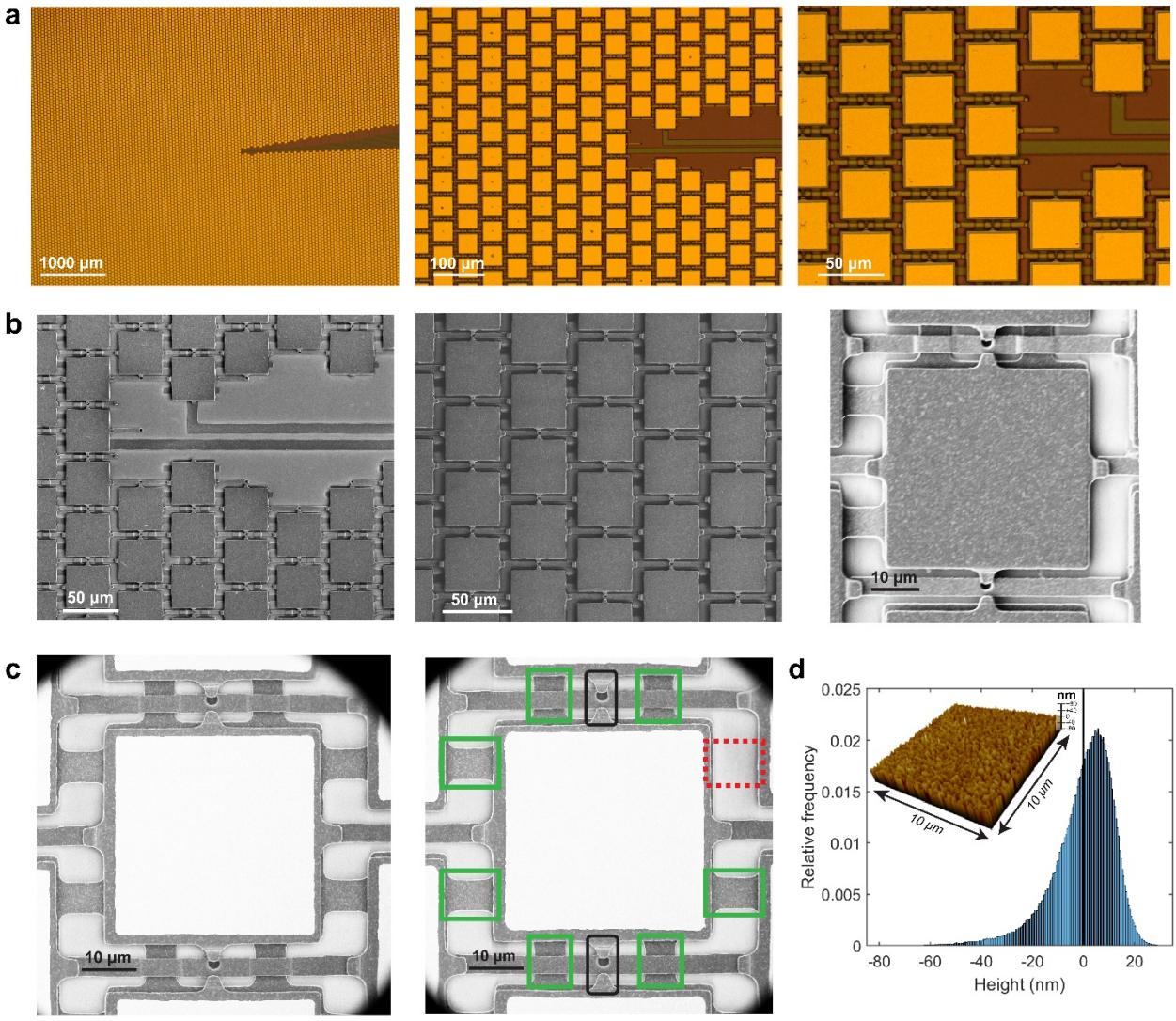

***Fig. 3**. Fabrication images of produced array. (**a**) Optical microscopy images of array center at various levels of zoom. (**b**) Scanning electron microscopy (SEM) images of array prior to metallization post-processing at various levels of zoom. (**c**) SEM images of two different pixels after metallization. Electrical wiring across pixels for grouped drive is achieved via 8 potential connections between fixed bottom electrodes at the Polysilicon 0 layer which can be added (green boxes, right image) or removed (red box, right image) in accordance with partitioning geometry. For each pixel, two Polysilicon 2 juts (black boxes, right image) hanging over the anchors of adjacent suspension beams serve as gap stop structures preventing electrode contact from electrostatic pull-in during operation. (**d**) Topography histogram of*

deposited reflective gold layer as measured by atomic force microscopy (AFM). Heights were measured per 50 nm x 50 nm region; histogram bin sizes are 0.5 nm. Top-left inset is a sample 2-dimensional topography plot across an area of 10 µm x 10 µm.

Array-level fabrication

The circular array was chosen to have a 32-ring partitioning geometry and an aperture diameter of 8.2 mm (for a total count of 23 852 pixels) based on an iterative optimization process using a previously described optical simulation framework that can assess axial focusing range with respect to axial resolution[41]. A 32-ring addressing scheme was chosen to maximize compatibility with a 32-channel commercial DAC system that was selected for array driving. As shown in Fig. 4a, ring-level track widths were gradually reduced with increasing ring radius in order to account for the sharper radial gradients produced at the edges of the array during axial focusing. Impedance measurements were also performed for each ring to assess driver requirements and inspect for shorting. In accordance with the parallel plate structure of the micromirrors, measured impedances were purely capacitive, with the capacitance of each ring closely following pixel count. Capacitance was generally found to increase with ring radius, and therefore also with ring area, and capacitance drops were noted between consecutive rings where track width was reduced (Fig. 4b). A linear regression of measured capacitance to pixel count had an R^2 of 0.98, further illustrating the correlation between the two properties. From the regression, mean pixel capacitance was evaluated to be 0.22 pF whereas mean parasitic capacitance due to traces and bond pads (seen in Fig. 4c) was 26.9 pF/ring. The measured pixel impedance is largely due to the mutual capacitance that exists across the nitride layer between the driving electrode in the Polysilicon 0 layer and the underlying single-crystal silicon which was grounded via nitride breach structures demarcated in Fig. 4c. A Polysilicon 0 layer wall surrounding the entire array was also

deposited to maintain uniform actuation behavior by shielding micromirrors from any potential residual stress mismatches across the bottom-most layers of the fabrication process[30] as well as to provide a ground connection to all micromirror bodies. A post-assembly image of a single 1 cm x 1 cm array chip is shown in Fig. 4d.

Pixel-level and ring-level performance

Following assembly, pixel-level functionality was evaluated using digital holographic microscopy[42]. Variation in the resting height of pixels across the array was found to have a standard deviation of 13.83 nm, indicating that the impact of beam buckling is minimal relative to the target displacement range of 550 nm. Steady state micromirror displacement was then measured as a function of applied voltage (Fig. 5a). In order to compactly quantify the actuation behavior of each pixel, the results were fit to a generalized form of the analytical solution to parallel plate capacitive transduction:

$$V = \sqrt{\boldsymbol{a}x(\boldsymbol{b} - \Delta x)^2}$$

This fit reduces all relevant geometric and material parameter values of each pixel down to two parameters *a* and *b* that accurately capture differences in actuation behavior due to regional process variations, as evidenced by the fact that the R^2 value of all fits exceed 0.99. Based on average actuation behavior, mean applied voltage for a displacement of 550 nm, i.e. 2π phase shift at wavelength of 1 100 nm, was 29.65 V while pull-in was found to occur at a mean voltage of 30.35 V. The parameter *b*, which corresponds to the effective electrode gap distance, was also assessed to be 2.16 µm, an 8% deviation from the nominal process value of 2 µm.

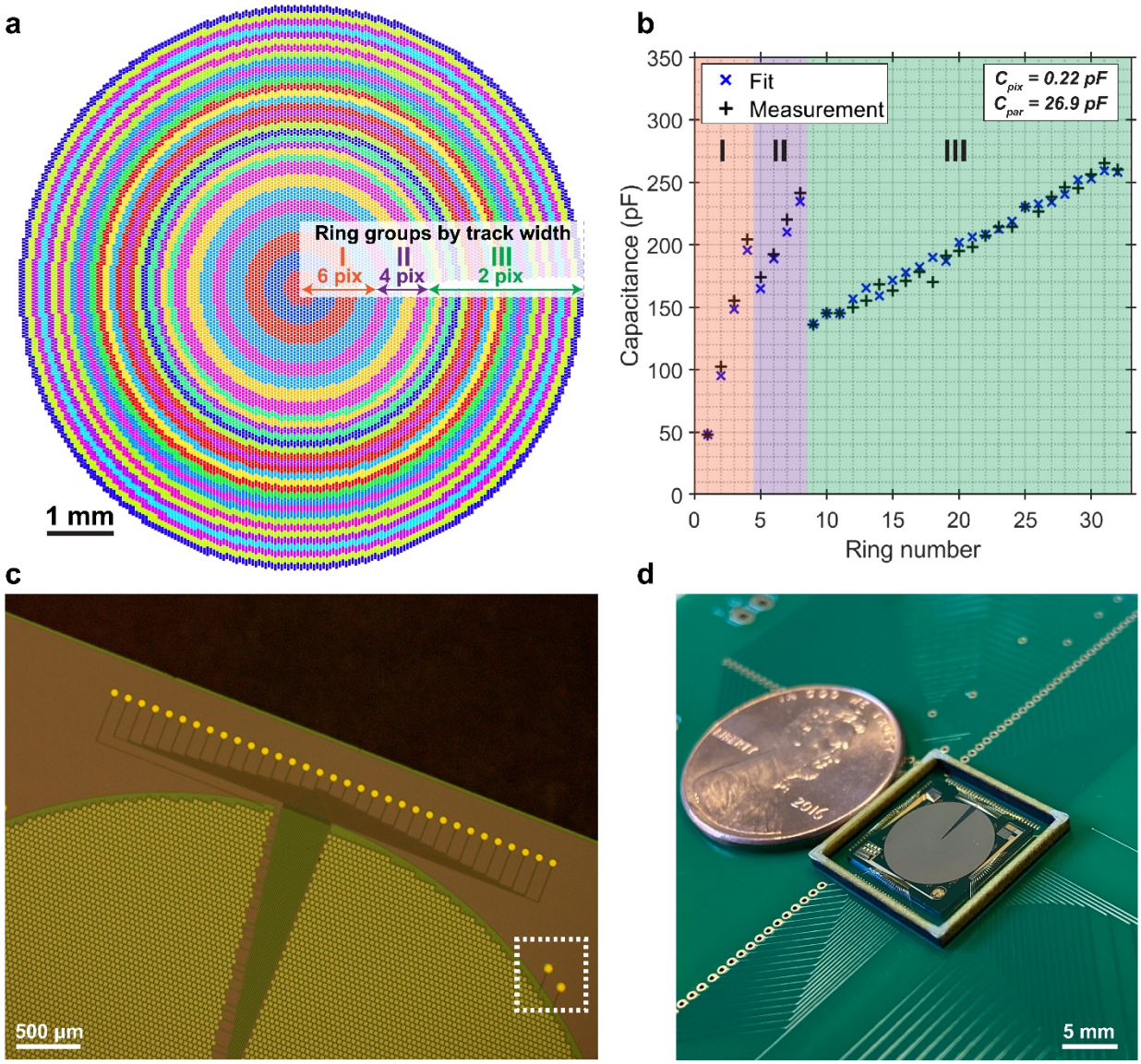

Fig. 4*. The selected wiring scheme determines driving requirements for the array. (**a**) Fabricated arrays were partitioned into 32 rings with track widths that decrease with increasing radius in order to account for the radial slope of applied spherical phase profiles. (**b**) Measured capacitance measurements of each ring. (**c**) Microscopy image showing the employed wiring scheme. Nitride breach structures (demarcated here with a white dashed box) were also used to ground the substrate (**d**) Photograph of mounted and assembled array chip next to US penny.*

Dynamic pixel behavior was subsequently characterized by measuring settling responses to various voltage steps under a stroboscopic setup as shown in Fig. 5b. All voltage steps were set to have an amplitude of 10 V, and the non-linear nature of the actuation behavior was exploited to achieve varying magnitudes of displacement by modifying the starting voltage offset from 0 V to 5 V and 20 V. The obtained measurements reveal an overdamped response with a settling duration that remains fairly consistent across changing magnitudes and directions in voltage step. Under a 2% settling time metric, mean response time was measured to be 114 μs for a refresh rate of 8.75 kHz. And under a 10-90% settling metric for suitable comparison against alternative approaches to axial focusing, mean response time was measured to be 64.8 μs for a refresh rate of 15.44 kHz, which is roughly two orders of magnitude faster than current commercial optofluidic and liquid crystal-based varifocal systems[9,15]. Overall, these response measurements demonstrate operating speeds that match the ~10 kHz benchmark achieved by galvanometer mirrors and that could be even raised further under optimized damping conditions.

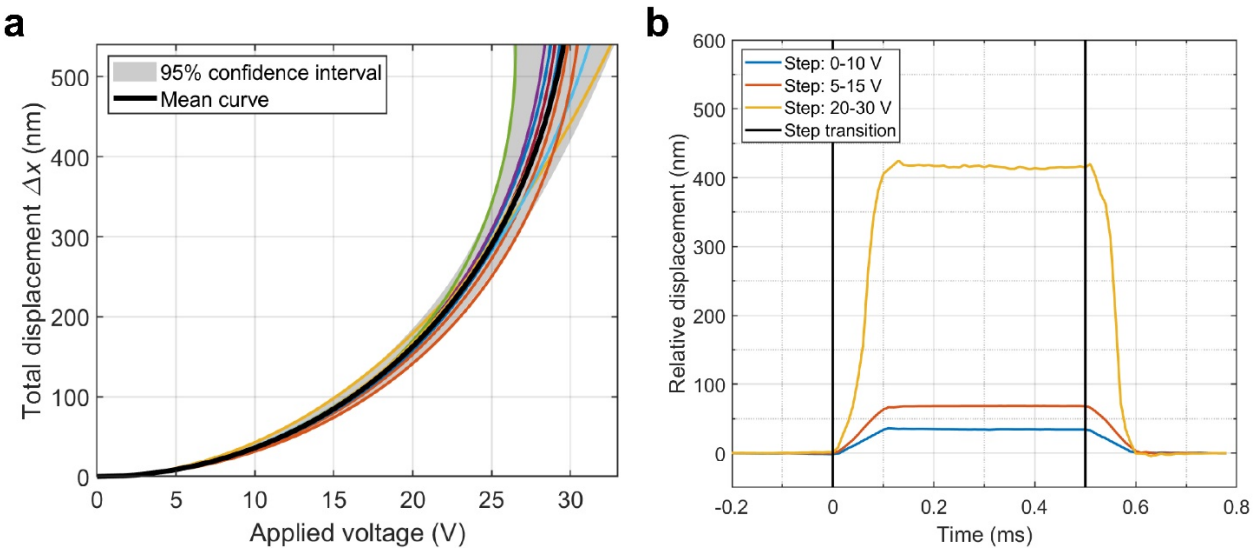

Fig. 5*. Pixel-level steady state and dynamic transduction characterization results obtained via digital holographic microscopy. (**a**) Measured steady state displacement vs applied voltage. Colored curves correspond to individual pixel measurements from various pixels across array. (**b**) Mean settling behavior of pixels measured stroboscopically by applying 1 kHz square wave voltage signals with a 10 V step and varying offsets for increasing ranges of displacement.*

Ring-level operation was also visualized across a large field of view (FOV) under digital holographic microscopy as shown in Fig. 6. While the increased FOV cannot resolve micromirror features well enough to accurately reconstruct and quantify pixel-level phase, ring-level actuation can be qualitatively evaluated for a single ring subjected to step-wise increases in applied voltage (Fig. 6a-f) as well as for several rings being actuated with the same voltage (Fig. 6g-h). Altogether, these phase reconstruction images serve to confirm that the employed wiring scheme results in coordinated and uniform co-actuation between pixels belonging to the same ring.

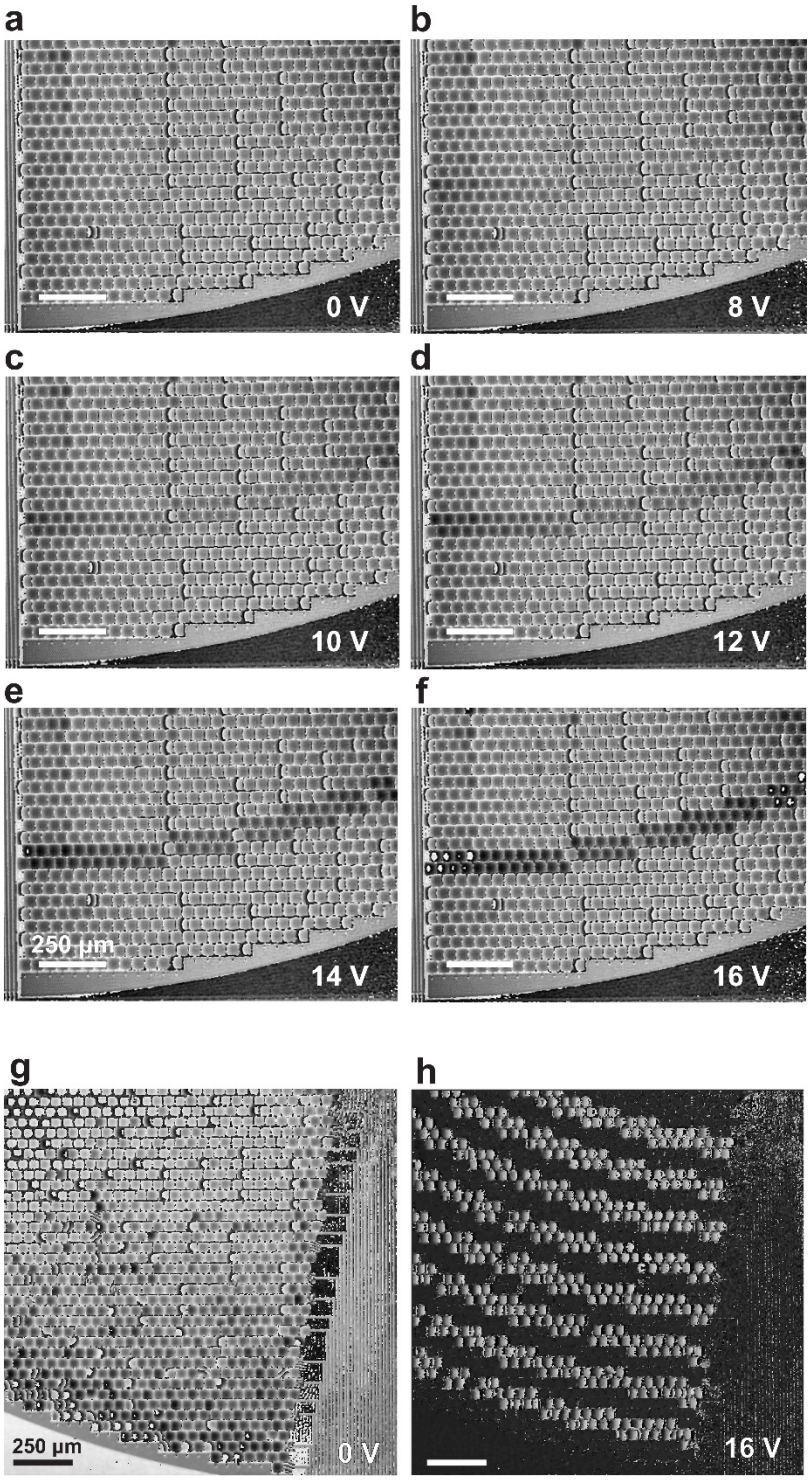

Fig. 6*. Phase reconstruction images obtained via digital holographic microscopy demonstrating ring-level actuation of array (all scale bars are 250 µm). (**a-f**) A single ring (#28 of 32 from center) was actuated in increasing steps with applied voltages of 0, 8, 10, 12, 14 and 16 V. (**g-h**) Alternating rings (#17, #19, #21,*

*#23, #25, #27, #29, and #31 from center) were concurrently actuated with an applied voltage of 16 V. (**g**) Phase reconstruction before actuation. (**h**) Phase difference after actuation.*

Array-scale axial focusing performance

Once pixel-level and ring-level functionalities were verified, array-scale axial focusing performance was evaluated using the test setup illustrated in Fig. 7. The optical setup consists of a collimated illumination sub-system involving two laser sources (532 nm and 980 nm wavelengths) as well as a *2f* optical configuration around an offset lens L2 (100 mm focal length) with the micromirror array at the front focal plane. A CMOS camera mounted on an automated z-stage and centered at the rear focal plane of L2 was used to acquire z-stacks for each phase profile applied using the array. To generate these phase profiles, the array was driven using 32 DACs with a 14-bit level of precision that can accommodate the sensitive higher-voltage region of the non-linear micromirror actuation curve. The mapping between desired phase and applied voltage was adjusted to the wavelength of the selected laser source such that a total drive of 29 V was required at 980 nm and 24.3 V was required at 532 nm. From the acquired z-stacks, lateral and axial projections of peak intensity values were used to quantify performance metrics including axial spot size, focusing range, lateral spot size, and deviations from the optical axis and target depth planes. Two folding mirrors M1 and M2 were used to multiplex test setup operation across four configurations, with M1 selecting between the two laser sources. Positioned to fold into place right in front of the array, M2 generates a single passive focus spot (at the rear focal plane z=0) which is used as a reference to assess the insertion loss of the micromirror array.

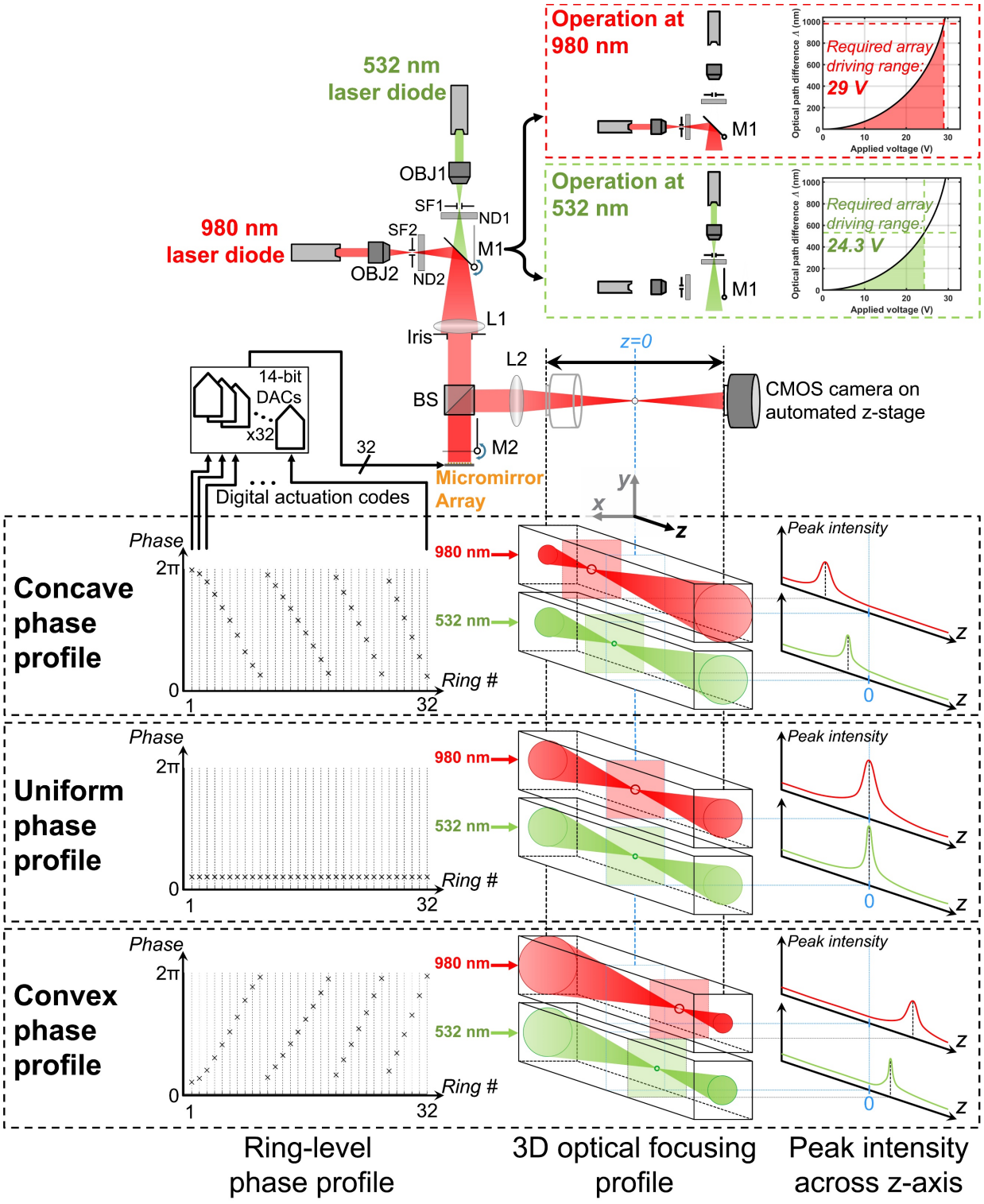

Fig. 7. *Schematic diagram of optical test setup, performed measurements, and drive electronics. For two distinct laser source wavelengths (532 nm and 980 nm), multiple phase masks corresponding to different*

target depths along the optical axis z were applied by driving the rings of the micromirror array with 32 DACs. Mirror M1 was employed to switch between laser sources. Mirror M2 was employed to alternate reflection between micromirror array and plain mirror in order to assess focusing efficiency η. A CMOS camera mounted on an automated z-stage was employed to acquire z-stack images across the full focusing range. For a given convex or concave phase mask, operation at 980 nm results in a greater focusing power and a larger spot size compared to operation at 532 nm. (OBJ: objective, SF: spatial filter, ND: neutral density filter, M: mirror, L: lens, BS: beamsplitter).

Despite the testing specificity imposed by the choice of laser wavelengths and of a particular focal length *f* for L2, system- and magnification-agnostic metrics may be extrapolated by exploiting the colinear scaling that governs focusing range and spot size. Focusing is determined by the relationship:

$$d_o \cdot d_i = f^2$$

where d_o is the distance from the micromirror at the rear focal plane to the focus spot in the object plane, and d_i is the distance from the rear focal plane to the focus spot in the image plane. And axial spot size is proportional to:

$$n\frac{\lambda}{NA^2} \propto \frac{\lambda \cdot f^2}{n \cdot D^2}$$

where λ corresponds to laser wavelength, *n* corresponds to the medium's refractive index, NA corresponds to the system's numerical aperture, and *D* corresponds to the aperture diameter set by the size of the micromirror array ($NA \approx 0.5\, nD/f$ under the low NA regime that is being considered). Accordingly, given the mutual scaling with f^2, the ratio of axial spot size to axial focusing range is intrinsic to the micromirror array and serves to measure the number of distinct, resolvable depth planes that the array can produce. Moreover, focusing range is bounded by the extent of 2π-wrapping present in the

phase profile produced by the array, which in turn scales with wavelength λ as evidenced by the following relationship determining the phase shift $\Delta\Phi$ required at a location (*x,y*) on the array:

$$\Delta\Phi(x,y) = 2\pi \frac{d_0 - d_0\sqrt{1 - \frac{(x^2+y^2)}{d_0^2}}}{\lambda}$$

Thus, in addition to being agnostic to focal length *f*, this range-to-spot size metric remains conserved across wavelengths assuming minimal impact from non-idealities in the array and lens L2. For this metric, spot size is quantified as the full width at half maximum (FWHM) while axial focusing range is quantified as the range across which peak intensity of the desired focus spot exceeds that of undesired higher-order diffraction effects.

Simulated and measured axial focusing performance at both 532 nm and 980 nm wavelengths are presented in Fig. 8a,b. The decreased efficiency that accompanies the higher phase gradients produced when targeting depths further away from the rear focal plane[26] can be observed in the simulation results and is reflected in the experimental data. This indicates that efficiency is primarily dependent on the discrete nature of ring-level phase steps and not pixel-level variation in actuation behavior. While simulation places zeroth-order diffraction efficiency under a uniform phase profile at 52%, consistent with the principle that it should theoretically be equal to the square of fill factor[33], measured efficiencies at 532 nm and 980 nm were 12.3% and 24.3%, respectively. These additional losses can be attributed to the reflectivity of the thinned gold layer as previous characterizations of gold films of similar thickness are in agreement with the fold changes in efficiency seen between measurement and simulation at both wavelengths[43]. A three-dimensional visualization of focusing performance is also provided with the lateral projections of acquired z-stacks in Fig. 8c,d. The appearance of faint spots at locations that are bilaterally symmetric to target depth planes with respect to the rear focal plane is most likely the result

of a small subset of hypersensitive pixels in each ring that effectively behave under binary operation much like zone plates[36].

Quantifications of axial and lateral positions of generated spots (Fig. 8 e,f) demonstrate the absence of significant lateral deviations from the optical axis as well as good agreement between targeted and obtained depths. The appearance of some slight deviation in axial position around the most negative target depth values also illustrates how calibration using such measurements provides a straightforward opportunity for the micromirror array to identify and tackle any system-specific rotationally symmetric aberration via the adjustment of a lookup table for ring-level actuation codes. Finally, with axial spot size across the focusing range measured to be 929 ± 195 μm (mean ± standard deviation) and focusing range evaluated to be 27.5 mm at a 532 nm wavelength, axial range-to-spot size ratio was calculated to be 29.6. While this represents a drop from the simulated ratio value of 37.6 resulting from a slight degradation in axial spot size due to pixel-level variations in actuation behavior, the array's demonstrated ability to resolve this many distinct depth planes comfortably meets requirements across several applications in fields including biological microscopy[44] and material processing[5].

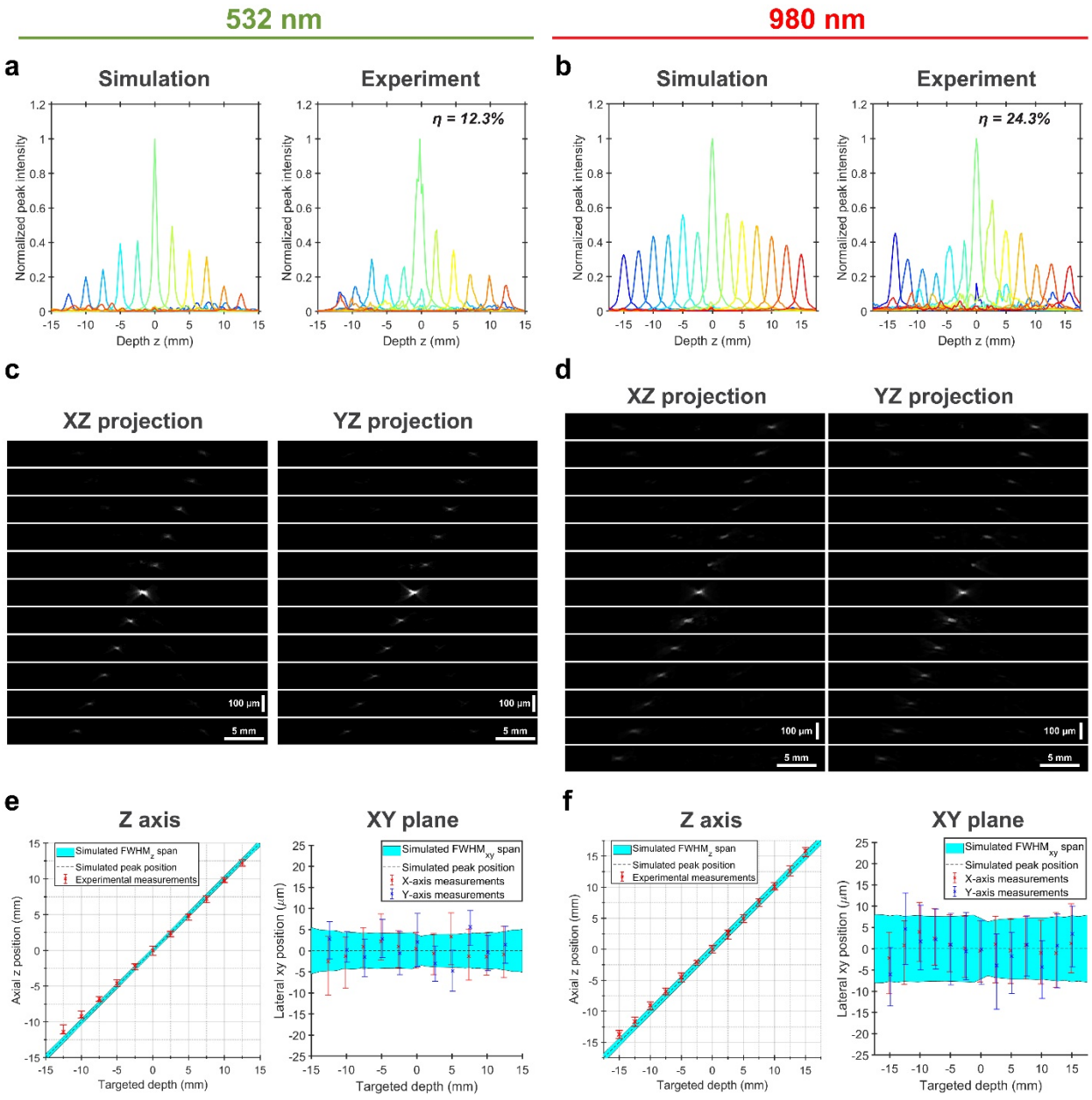

Fig. 8. *Optical focusing performance results. (**a-b**) Simulated and experimental results of peak intensity values projected along the optical axis for 532 nm (**a**) and 980 nm (**b**) sources. Each colored line corresponds to a distinct applied phase mask, efficiency η included as inset. (**c-d**) Lateral projections of acquired Z-stacks along XZ plane and YZ plane for all applied phase masks with 532 nm (**c**) and 980 nm (**d**) sources. Scales for lateral dimensions (X and Z) differ from Z-axis scales as indicated by provided scale bars. (**e-f**) Spot size and position measurements along X, Y and Z dimensions compared against simulated*

*values for 532 nm (**e**) and 980 nm (**f**) sources. Spans of measurement bars and simulation envelopes correspond to spot size values measured as full width at half maximum. X-shaped measurement markers correspond to peak intensity position along z for left side plots and peak intensity distance from optical axis for right side plots.*

Discussion

Whether applied under an adaptive optics framework for defocus correction or in a 3D translation context for depth targeting, axial focusing constitutes a fundamental and ubiquitous mode of optical manipulation. Fittingly, the micromirror array presented in this work achieves axial focusing capabilities suitable for general-purpose use by exploiting the robustness of this fundamental phase mode to alleviate driving burden. By adopting an architecture that reserves phase accuracy for the outer regions of the active area, allows for radial phase-wrapping, and relaxes uniformity in favor of sensitivity, the described array reached a refresh rate of ~10 kHz across wavelengths of up to 1 100 nm, with only 32 addressing channels and <30 V of required drive. Furthermore, this performance was achieved without the hindrance of constraints such as polarization dependence, continuous sweeping and non-ideal radial phase curvatures.

Taken together, these performance capabilities can potentially eliminate bottlenecks across several applications. For instance, the achieved axial range-to-spot size ratio of 29.6 exceeds the requirements imposed by optical systems involving either neural stimulation or recording, where neuron targets have sizes on the order of 10 μm^6 and scattering under linear one-photon regimes limit accessible depth to ~100 µm. More pertinently to state-of-the-art systems, the axial confinement offered by multi-photon regimes that extend accessible depths to ~1 mm can also be exploited to relax axial resolution and achieve single-cell full-range targeting at speeds that exceed the characteristic ~1 kHz benchmark of

neural signaling[7]. Alternatively, in the field of augmented and virtual reality, where varifocal tools are mandated for the prevention of vergence-accommodation conflicts[2], the proposed tool can be especially nimble in exploiting the window across which the human eye integrates kHz-speed physiological detections for an effective perception rate of ~100 Hz[8]. Specifically, the array could be used to either partition complex 3D images into simpler frames, couple in lateral scanning tools, or multiplex light sources, all without any restriction on the order and duration of targeted depths[8].

Despite the high speeds associated with MEMS-based approaches, the inertial nature of mechanical moving systems has spurred parallel efforts favoring solid-state mechanisms for optical manipulation[14]. Namely, acousto-optic and electro-optic modulation approaches, which offer refresh rates of up to 1 MHz[14], have become increasingly popular in recent years with the widespread adoption of tools such as acousto-optic deflectors for lateral scanning[45]. Unfortunately, this benefit of ultrafast responsivity has not translated into viable high-speed axial focusing as limitations in control and sensitivity result in performance costs such as drastic insertion loss[46] or high voltage drive requirements[47]. In addition, MEMS structures have the distinct advantage of being ideal dynamic substrates for metamaterials. Functional metasurfaces such as metalenses offer the potential for compact and highly-tailored functionality in future generation optical systems. But their inherently passive nature requires the use of complementing active elements which typically become sources of performance bottleneck. With MEMS-based dynamic substrates, such shortcomings related to response times and fabrication compatibility can be circumvented[48,49].

While the strategy of increasing micromirror sensitivity for reduced voltage drive in this work does lead to more variation in actuation behavior across pixels, the reported functional testing results demonstrate that these mismatches do not significantly affect axial focusing performance. These pixel-level disparities in actuation can be directly attributed to geometric and process-related properties, most importantly electrode gap thickness, suspension beam thickness, and residual stress. And since

die-level variations of these properties exhibit spatial continuity, the potential for regional drive correction (akin to calibration approaches in full-fledged spatial light modulators)[50] opens up opportunities for expanded phase control using similar low-voltage pixel structures.

Another design tradeoff concession made in order to maximize fill factor while abiding by planarity constraints was the use of two suspension beams per pixel instead of three or four. This structural limitation, which introduces an unconstrained torsional degree of freedom, was mitigated with the incorporation of gap stops to prevent electrode contact in the event of tilting and was not found to significantly degrade lateral spot size along any specific orientation. And similarly to pixelated spatial modulator arrays, the presented axial focusing array's reliance on discrete phase steps results in target depth-dependent efficiency[26]. Though this efficiency profile may not be ideal for applications that require uniform intensity across depth, the axial operating range can be restricted to a region across which efficiency variation is less extensive as evidenced by the 980 nm focusing performance results (Fig. 8b). While the overall impact of torsional freedom and efficiency on the functional performance of the varifocal array remains limited, the need for concessions such as these can be obviated in future design iterations by expanding the fabrication process. Specifically, a planarization step could decouple the suspension network from the active area, thereby offering increased space for both additional suspension beams and higher fill factors. Given that no significant mirror curling was observed, the thickness of the reflective layer may also be increased for improved reflectivity[43].

Altogether, the axial focusing tool presented in this work constitutes both a versatile product and an attractive platform for expanded or reconfigured optical modulation. For the current array embodiment, the light operating overhead that the 30 V, 32-channel driving scheme represents makes compact on-board driver integration feasible. With a reduced wavelength range requirement, driving ranges can be lowered even further by applying a negative voltage bias to suspended mirror bodies: halving the wavelength range from 1 100 nm to 550 nm would, for instance, reduce driving voltages to less than 8 V

under this approach. Moreover, the systematic nature of the pixel wiring process offers a straightforward pathway from general-purpose to application-specific design that may involve modifications in aperture size, reconfigurations to the partitioning scheme, or readjustments to the number of addressable channels[41]. Finally, this micromirror platform can potentially accommodate expanded features such as limited dynamic partitioning via relays outside of the active area.

Materials and methods

Design, fabrication and assembly of array

The array-scale geometry of the axial focusing tool was designed using a previously described custom simulation framework[41]. Reflective pixel elements were placed in the active region of the computational framework in accordance with the chosen tiling scheme and sorted into elemental rings. The final 32-channel partitioning arrangement and aperture size were chosen based on an iterative process involving regrouping these elemental rings and evaluating focusing performance. The pixel-level micromirror structure was developed using analytical simulations of parallel-plate capacitive transduction as well as finite element analyses.

The arrays were fabricated using the standard PolyMUMPs service offered by MEMSCAP (Durham, NC, USA). As part of MEMSCAP's MUMPs-PLUS option, the Polysilicon 1 layer was modified from the 2 µm standard of the PolyMUMPs process to 0.5 µm. To ensure micromirror reflectivity while minimizing residual stress effects, the 500 nm gold layer offered as part of the PolyMUMPs process was avoided in favor of a 250 nm thick gold layer that was custom-deposited during in-house post-processing via lift-off and evaporation. Following oxide release, array chips were mounted and wire-bonded to custom printed circuit boards (PCBs) via epoxy-based attaching and gold ball bonding.

Micromirror array inspection

Released, standalone array chips were examined under optical microscopy, scanning electron microscopy, and atomic force microscopy. AFM was performed in non-contact mode to assess the topography of the deposited reflective gold layer. Heights were measured per 50 nm x 50 nm region across several pixels and a total area of 190 μm^2. Impedance measurements were also performed on released array chips at a frequency of 1 kHz and under a parallel Cp-Rp model using an LCR Meter and a micromanipulator probe station for direct access to bond pads.

Array driving

The micromirror array was driven with a 32-channel 14-bit precision DAC. A commercial FPGA programmed with custom firmware was used for digital interfacing between DAC and software for operation. Digital and analog power supplies were provided to the DAC using a power supply and a precision source/measure unit. The 32 voltage outputs of the DAC (along with ground) were connected to the micromirror array PCB via ribbon cable.

Digital holographic microscopy

Digital holographic microscopy was performed on assembled arrays in ambient air at room temperature for phase and amplitude reconstruction using a 675 nm wavelength laser source under a reflection-based interferometric scheme[42]. While steady state measurements were performed using DAC voltage outputs, dynamic measurements were performed using a stroboscopic unit, which employs a dedicated voltage output (10 V maximum swing with 2% accuracy) for synchronization to laser pulses. Offsets of 0

V, 5 V and 10 V were applied with a 10 V amplitude to access different regions of the non-linear micromirror actuation curve and evaluate step responses across small and large displacement ranges. The stroboscopic unit achieves precise measurements of MHz-regime mechanical actuation speeds by applying a periodic drive, applying nanosecond-regime laser pulses at specific time offsets of the periodic signal, and integrating the signal from several periods spanning the camera's shutter time for adequate SNR. Specifically, micromirror settling behavior was reconstructed from stroboscopic acquisition runs employing a 1 kHz square wave driving signal and with an effective sampling rate of 100 kHz.

Optical testing of focusing performance

Functional performance of the axial focusing array was evaluated under the optical test setup illustrated in Fig. 7 in ambient air at room temperature. A camera was mounted on a motorized linear stage for 12-bit z-stack acquisitions of each applied phase. The step size of the linear stage, i.e. the axial precision of the acquisition, was set to 200 µm. FPGA-mediated DAC voltage drive, camera acquisition and stage control were coordinated for automation using custom software. Collimated laser modules were used as the 532 nm wavelength and the 980 nm wavelength laser sources. An achromatic doublet with a focal length of 100 mm was used as the offset lens for axial focusing. To ensure measurement accuracy, four acquisition runs were performed and averaged for each applied phase profile. Efficiency was assessed by integrating pixel intensities across the zeroth-order spot produced by the micromirror array as well as the focus spot produced by the plain reference mirror. Efficiency was subsequently calculated by taking the ratio between the two integrated intensities and multiplying this ratio with the reflectance of the plain mirror at the wavelength under study. For each wavelength, a geometric mean of z-stacks across all applied phase profiles was used to subtract out background, back-reflections from flat optical

elements and static reflections from non-active areas of the array chip. The optical axis was determined in the z-stacks by performing linear regressions of the X and Y positions of the peak intensity values from each applied phase profile to their depth position Z. Lateral spot size was obtained at the peak intensity depth plane by estimating the FWHM along X and Y axes via spline interpolation. Similarly, axial spot size was determined for each target spot by generating a profile of peak intensity at each depth and estimating the FWHM from this profile via spline interpolation.

Data and code availability

Measurement data as well as firmware and software code can be made available upon request.

Acknowledgements

The authors thank Prof. Ming Wu, the Marvell Nanofabrication Laboratory, Mohammad Meraj Ghanbari, sponsors of the Berkeley Wireless Research Center, and sponsors of the Berkeley Sensor & Actuator Center for tools, equipment and helpful discussions. We are grateful to V. Aksyuk (NIST) for useful discussions and to D. Czaplewski from Argonne National Laboratory for his help with the metallization process. This work was performed, in part, at the Center for Nanoscale Materials, a U.S. department of Energy Office of Science User Facility, and supported by the U.S. Department of Energy, Office of Science, under Contract No. DE-AC02-06CH11357.

Conflict of interests

The authors have no conflicts of interest to report.

Contributions

NTE designed the micromirror device, performed characterization and testing, analyzed results, and wrote the manuscript. CY contributed to concept development, and built the firmware and software for DAC-based voltage drive. NA was the main contributor to the design and assembly of the optical test setup. NP contributed to concept development and provided the basis for the computational design framework. LW contributed to concept development, and provided resources for optical testing. DL contributed to concept development, MEMS design and fabrication (including post-processing), and array inspection under optical microscopy. RM contributed to concept development, provided electronic resources for driving and characterization, supervised the execution of this work overall, and edited the manuscript. All authors also provided manuscript feedback.

References

1. Žurauskas, M., Barnstedt, O., Frade-Rodriguez, M., Waddell, S. & Booth, M. J. Rapid adaptive remote focusing microscope for sensing of volumetric neural activity. *Biomed. Opt. Express* **8,** 4369 (2017).

2. Dunn, D. *et al.* Wide field of view varifocal near-eye display using see-through deformable membrane mirrors. *IEEE Trans. Vis. Comput. Graph.* **23,** 1322–1331 (2017).

3. Grulkowski, I. *et al.* Swept source optical coherence tomography and tunable lens technology for comprehensive imaging and biometry of the whole eye. *Optica* **5,** 52–59 (2018).

4. Matthews, S. A., Collados, M., Mathioudakis, M. & Erdelyi, R. The European solar telescope (EST). in *Ground-based and Airborne Instrumentation for Astronomy VI* **9908,** 990809 (International Society for Optics and Photonics, 2016).

5. Chen, T.-H., Fardel, R. & Arnold, C. B. Ultrafast z-scanning for high-efficiency laser micro-machining. *Light Sci. Appl.* **7,** 17181 (2018).

6. Meitzen, J., Pflepsen, K. R., Stern, C. M., Meisel, R. L. & Mermelstein, P. G. Measurements of neuron soma size and density in rat dorsal striatum, nucleus accumbens core and nucleus accumbens shell: differences between striatal region and brain hemisphere, but not sex. *Neurosci. Lett.* **487,** 177–181 (2011).

7. Wang, T. *et al.* Quantitative analysis of 1300-nm three-photon calcium imaging in the mouse brain. *Elife* **9,** e53205 (2020).

8. Borghuis, B., Tadin, D., Lankheet, M., Lappin, J. & van de Grind, W. Temporal Limits of Visual Motion Processing: Psychophysics and Neurophysiology. *Vision* **3,** 5 (2019).

9. Bathe-Peters, M., Annibale, P. & Lohse, M. J. All-optical microscope autofocus based on an electrically tunable lens and a totally internally reflected IR laser. *Opt. Express* **26,** 2359–2368 (2018).

10. Ozbay, B. N. *et al.* Miniaturized fiber-coupled confocal fluorescence microscope with an electrowetting variable focus lens using no moving parts. *Opt. Lett.* **40,** 2553–2556 (2015).

11. Wang, L., Hayakawa, T. & Ishikawa, M. Dielectric-elastomer-based fabrication method for varifocal microlens array. *Opt. Express* **25,** 31708–31717 (2017).

12. Wang, Y.-J., Hsieh, H.-A. & Lin, Y.-H. Electrically tunable gradient-index lenses via nematic liquid crystals with a method of spatially extended phase distribution. *Opt. Express* **27,** 32398–32408 (2019).

13. Iwai, D., Izawa, H., Kashima, K., Ueda, T. & Sato, K. Speeded-Up focus control of electrically tunable Lens by Sparse optimization. *Sci. Rep.* **9,** 1–6 (2019).

14. Römera, G. & Bechtoldb, P. Electro-optic and acousto-optic laser beam scanners-Invited Paper. *Phys. Procedia* **56,** 29–39 (2014).

15. Zhang, Z., You, Z. & Chu, D. Fundamentals of phase-only liquid crystal on silicon (LCOS) devices. *Light Sci. Appl.* **3,** e213–e213 (2014).

16. Chakraborty, T. *et al.* Converting lateral scanning into axial focusing to speed up 3D microscopy. *bioRxiv* (2020).

17. Arnold, C. B., Theriault, C., Amrhein, D., Kang, S. & Dotsenko, E. Ultra-high-speed variable focus optics for novel applications in advanced imaging. in *Photonic Instrumentation Engineering V* (ed. Soskind, Y. G.) **10539,** 1 (SPIE, 2018).

18. Shao, Y., Dickensheets, D. L. & Himmer, P. 3-D MOEMS mirror for laser beam pointing and focus control. *IEEE J. Sel. Top. Quantum Electron.* **10,** 528–535 (2004).

19. Janin, P., Bauer, R., Griffin, P., Riis, E. & Uttamchandani, D. Characterization of a Fast Piezoelectric Varifocal MEMS Mirror. in *2018 International Conference on Optical MEMS and Nanophotonics (OMN)* 1–5 (IEEE, 2018). doi:10.1109/OMN.2018.8454626

20. Dwight, J. G. & Tkaczyk, T. S. Lenslet array tunable snapshot imaging spectrometer (LATIS) for hyperspectral fluorescence microscopy. *Biomed. Opt. Express* **8,** 1950–1964 (2017).

21. Ronzitti, E. *et al.* Submillisecond Optogenetic Control of Neuronal Firing with Two-Photon Holographic Photoactivation of Chronos. *J. Neurosci.* **37,** 10679–10689 (2017).

22. Solgaard, O. *Photonic microsystems: Micro and nanotechnology applied to optical devices and systems*. (Springer Science & Business Media, 2009).

23. Brubaker, N. D., Siddique, J. I., Sabo, E., Deaton, R. & Pelesko, J. A. Refinements to the study of

electrostatic deflections: theory and experiment. *Eur. J. Appl. Math.* **24,** 343–370 (2013).

24. Liu, T., Rajadhyaksha, M. & Dickensheets, D. L. MEMS-in-the-lens architecture for a miniature high-NA laser scanning microscope. *Light Sci. Appl.* **8,** 1–11 (2019).

25. Hamann, S. & Solgaard, O. Variable Focusing and Steering Using High Speed MEMS Phased Array. in *2018 International Conference on Optical MEMS and Nanophotonics (OMN)* 1–2 (2018). doi:10.1109/OMN.2018.8454579

26. Blanche, P.-A. Introduction to Holographic. in *Optical Holography-Materials, Theory and Applications* 1–39 (Elsevier, 2020).

27. Yan, Y., Tian, X., Liang, R. & Sasian, J. Optical performance evaluation and chromatic aberration correction of a focus tunable lens used for 3D microscopy. *Biomed. Opt. Express* **10,** 6029–6042 (2019).

28. Salter, P. S. & Booth, M. J. Adaptive optics in laser processing. *Light Sci. Appl.* **8,** 1–16 (2019).

29. Li, X. *et al.* Adaptive optimization for axial multi-foci generation in multiphoton microscopy. *Opt. Express* **27,** 35948–35961 (2019).

30. Kumar, A., Bansal, D., Kumar, P. & Rangra, K. Post-release deformation and curvature correction of an electrothermally actuated MEMS bilayer platform. *Microelectron. Eng.* **221,** 111192 (2020).

31. Song, Y., Panas, R. M. & Hopkins, J. B. A review of micromirror arrays. *Precis. Eng.* **51,** 729–761 (2018).

32. Madec, P.-Y. Overview of deformable mirror technologies for adaptive optics and astronomy. in *Adaptive Optics Systems III* (eds. Ellerbroek, B. L., Marchetti, E. & Véran, J.-P.) **8447,** 844705-844705–18 (International Society for Optics and Photonics, 2012).

33. Martínez, A., del Mar Sánchez-López, M. & Moreno, I. Phasor analysis of binary diffraction gratings with different fill factors. *Eur. J. Phys.* **28,** 805 (2007).

34. Zhang, H., Xie, J., Liu, J. & Wang, Y. Elimination of a zero-order beam induced by a pixelated spatial light modulator for holographic projection. *Appl. Opt.* **48,** 5834–5841 (2009).

35. Marquez, A. *et al.* Amplitude apodizers encoded onto Fresnel lenses implemented on a phase-only spatial light modulator. *Appl. Opt.* **40,** 2316–2322 (2001).

36. Benton, D. M. Multiple beam steering using dynamic zone plates on a micromirror array. *Opt. Eng.* **57,** 1 (2018).

37. Madec, P.-Y. Overview of deformable mirror technologies for adaptive optics and astronomy. **8447,** 844705-844705–18 (2012).

38. Ryan, P. J., Cornelissen, S. A., Lam, C. V & Bierden, P. A. Performance analysis of two high actuator count MEMS deformable mirrors. in *MEMS Adaptive Optics VII* **8617,** 861705 (International Society for Optics and Photonics, 2013).

39. Watson, G. P. *et al.* Spatial light modulator for maskless optical projection lithography. *J. Vac. Sci. Technol. B Microelectron. Nanom. Struct. Process. Meas. Phenom.* **24,** 2852–2856 (2006).

40. Lapisa, M., Zimmer, F., Niklaus, F., Gehner, A. & Stemme, G. CMOS-integrable piston-type micro-mirror array for adaptive optics made of mono-crystalline silicon using 3-D integration. in *Proceedings of the IEEE International Conference on Micro Electro Mechanical Systems (MEMS)* 1007–1010 (2009). doi:10.1109/MEMSYS.2009.4805556

41. Ersumo, N. T. *et al.* Design Framework for High-Speed 3D Scanning Tools and Development of an Axial Focusing Micromirror-Based Array. in *MOEMS and Miniaturized Systems XIX, SPIE Opto* (2020).

42. Montfort, F. *et al.* Process engineering and failure analysis of MEMS and MOEMS by digital holography microscopy (DHM). in *Reliability, Packaging, Testing, and Characterization of MEMS/MOEMS VI* **6463,** 64630G (International Society for Optics and Photonics, 2007).

43. Dejene, F. B. & Ocaya, R. O. Electrical, optical and structural properties of pure and gold-coated VO2 thin films on quartz substrate. *Curr. Appl. Phys.* **10,** 508–512 (2010).

44. Pégard, N. C. *et al.* Three-dimensional scanless holographic optogenetics with temporal focusing (3D-SHOT). *Nat. Commun.* **8,** 1228 (2017).

45. Sancataldo, G. *et al.* Flexible multi-beam light-sheet fluorescence microscope for live imaging without striping artefacts. *Front. Neuroanat.* **13,** 7 (2019).

46. Reddy, G. D. & Saggau, P. Fast three-dimensional laser scanning scheme using acousto-optic deflectors. *J. Biomed. Opt.* **10,** 064038 (2005).

47. Park, S. *et al.* Electrically focus-tuneable ultrathin lens for high-resolution square subpixels. *Light Sci. Appl.* **9,** 1–13 (2020).

48. Arbabi, E. *et al.* MEMS-tunable dielectric metasurface lens. *Nat. Commun.* **9,** 812 (2018).

49. Roy, T. *et al.* Dynamic metasurface lens based on MEMS technology. *Apl Photonics* **3,** 21302 (2018).

50. Lazarev, G., Chen, P.-J., Strauss, J., Fontaine, N. & Forbes, A. Beyond the display: phase-only liquid crystal on Silicon devices and their applications in photonics. *Opt. Express* **27,** 16206–16249 (2019).